CONDENSATION AND ICING ON COOLED SURFACES

Gernot J. Pauschenwein, Scientist, Energy Department, Austrian Institute of Technology AIT, Vienna, Austria
Christoph Reichl, Scientist, Energy Department, Austrian Institute of Technology AIT, Vienna, Austria
Bernd Windholz, Junior Engineer, Energy Department, Austrian Institute of Technology AIT, Vienna, Austria
Immacolata Moretti, Junior Engineer, Energy Department, Austrian Institute of Technology AIT, Vienna, Austria
Michael Monsberger, Head of "Sustainable Thermal Energy Systems", Energy Department, Austrian Institute of Technology AIT, Vienna, Austria

Abstract: Condensation and subsequent icing are phenomena that have an influence on many applications, either as an intended process, like condensation in the heat extraction from exhausts of thermal power plants, or unwanted occurrence, for example at air-source heat exchangers for heat pumps, where accreted ice causes deteriorated performance and ultimately blockage of the whole device. There exist already thorough studies, on the growth of water films and ice layers on cooled surfaces, but what is still badly missing is a systematic investigation of the onset of condensation and icing. These onset processes are governed by the laws of heterogeneous nucleation, a theory which is not very well established for technological applications. Therefore the present work firstly consists of experiments on condensation and icing on cooled surfaces under varying conditions. Secondly, the captured experimental data are used as input for computational fluid dynamics simulations, coupled with a boundary condition for the cooled surface based on classical nucleation theory as a model for the onset of occurring water droplets and ice crystals.

Key Words: condensation, icing, heterogeneous nucleation, CFD

1 INTRODUCTION

In (Reichl et al. 2010) an experimental facility to investigate icing and condensation in low speed flows using thermographic and image capturing methods was presented. The facility was characterized with respect to local thermodynamic and flow properties using various experimental techniques including Constant Temperature Anemometry (CTA), three dimensional particle image velocimetry (3D-PIV), surface temperature sensors and heat sphere probes. The experimental setup and the most important results are summarized in the first part. We will include results from thermocouple and pt100 difference measurements. Then we will present a computational analysis method to gain insight into the data of the image capturing during the underlying phase change processes. This methodology is finally applied to plates and glasses exhibiting different surface structures.

The path to an understanding of condensation and icing starts at practical knowledge from field studies, which stimulate experimental investigations of condensation and ice accretion [see e.g. (Reichl et al. 2010, Piucco et al. 2008, Narhe and Beysens 2007, Wu et al. 2007, Shaw and Lamb 1999)]. The development of suitable models, in this paper through nucleation theory (see section 4.1), subsequently leads to investigations of the models via simulations, presented in section 4. Although there exist studies of the nucleation at surfaces

on a molecular level (Toxvaerd 2002), the current work does not aim at this nano-scale level, since it would be computationally impossible to simulate and describe macroscopic devices like heat exchangers with this detailed method.

The most detailed yet still applicable method of simulation in this case is the finite volume method of computational fluid dynamics (CFD), for which there exist various commercial and cost-free tools. Since the processes of nucleation, droplet and crystal growth and humidity transport are to be modelled, the open source code OpenFOAM (http://www.openfoam.com/) is used. It is open, not only in terms of source code, but also in its structure and hierarchical design, so that its solvers, utilities and libraries are fully extensible. Using these possibilities it is feasible to simulate not only the growth of films or frost layers (Lee et al. 2003), but really the physical behaviour at the onset of condensation or icing, i.e., the corresponding nucleation process, as will be shown in section 4.2.

2 NOMENCLATURE

$c_{\mathrm{m,v}}$	Vapor mass concentration
$D_{\mathrm{v}} = 2.12 \cdot 10^{-7}\,\mathrm{m^2/s}$	Diffusion constant of vapour in air
$d_1 \simeq \sqrt[3]{(6\mu_{\mathrm{H_2O}})/(\pi N_{\mathrm{A}} \rho_{\mathrm{H_2O}})}$	Approximate diameter of water molecule
$\Delta G^\star$	Gibbs free energy barrier for critical embryo
J	Nucleation rate
J_0	Kinetic constant of nucleation
$\mathbf{j}$	Vapor flux
$k_{\mathrm{B}} = 1.3806504 \cdot 10^{-23}\,\mathrm{J/K}$	Boltzmann constant
$\dot{m}/A$	Mass flux to the surface of nucleation
$N_{\mathrm{A}} = 6.0221415 \cdot 10^{23}\,\mathrm{mol^{-1}}$	Avogadro constant
$\mathbf{n}$	Unit vector normal to the surface of the flow region
P_{v}, $P_{\mathrm{v,sat}} = \mathrm{e}^{77.34 - 7235.42/(T/\mathrm{K}) - 8.2\log(T/\mathrm{K}) + 0.00571\,T/\mathrm{K}}$	(saturation) vapor pressure
$R = 8.314472\,\mathrm{J/(K\,mol)}$	Gas constant
$r^\star$	Critical embryo radius
S	Saturation ratio (relative humidity)
T	Temperature
$\mathbf{u}$	Flow velocity
$V^\star$, $V^\star_{\mathrm{het}}$	(heterogeneous) critical volume

Greek symbols:

$\mu_{\mathrm{H_2O}} = 18.0153\,\mathrm{g/mol}$	Molar mass of water
$\rho_{\mathrm{H_2O}} = (1049.572 - 0.1763\,T/\mathrm{K})\,\mathrm{kg/m^3}$	Density of liquid water
σ	Surface tension between water and air

3 EXPERIMENTS

To investigate condensation and icing on micro structured plates [frosting and defrosting of flat plates see e.g. (Aljuwayhel et al. 2007), (Lee at al. 2003), (Roy at al. 2005), (Egolf 1984), (Tassou and Marquand 1987), (Piucco et al. 2008), (Wu et al. 2007), (Lee et al. 2003)] an experimental test rig has been assembled, which consists of a wind tunnel driven by electronically controlled fans and a cooling circuit connected to a stainless steel support plate (see Figure 1). The support plate temperature can be adjusted in a range of -30 °C to +80 °C. The whole test rig is placed in a climatic chamber, which is capable of providing predefined and stable values of temperature and relative humidity. The phase change processes are monitored using "high-speed" and thermo-camera visualization techniques.

3.1 Experimental Setup

The experimental setup used for the phase change studies consists of a wind tunnel driven by fans. The temperature of the test section plate is controlled via an external heat exchanger unit (see Figure 1). The wind tunnel was constructed mainly using stainless steel and aluminium parts. The test section is covered using an acryl-glass part, which provides 3-side optical access. The cross section of the wind tunnel is 300 mm x 100 mm. The different flow fields are generated using three axial fans. They can be drive controlled using pulse width modulation providing a maximum volume flow of 500 m^3/h each (see Figure 1, left). An ultra-low-refrigerated circulator using the refrigerant R507 was used to keep the test section plate attached to the heat exchanger at constant temperature. The temperature control liquid is capable of stabilizing the temperature in a range of -30 °C to +80 °C. The cooling capacity of the heat exchanger unit is not constant with temperature (2000 W at +20 °C down to 260 W at -40 °C), while the heater capacity is 3000 W independent of the fluid temperature. The pump was set to its maximum, producing flow rates around 22 l/min. The heat exchanger circuit is stabilized in a range of ±0.05 °C using self-optimized intelligent cascade controlling.

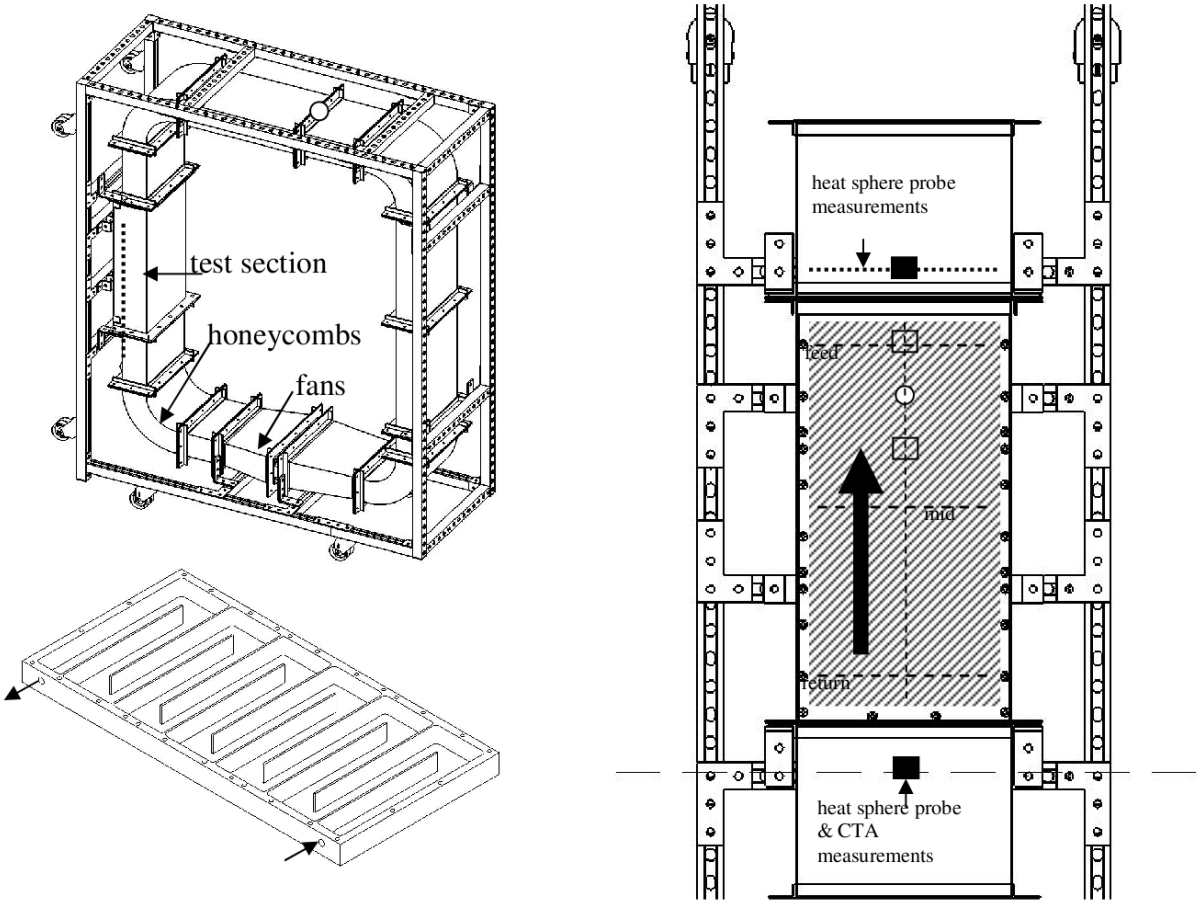

Figure 1. Experimental Setup. Upper left: inclined crack of the full closed channel setup. The dotted line marks the position of the heat exchanger unit. Lower left: heat exchanger unit (cover removed). The arrows show the fluid flow direction. Right: front view of the test section (hatched area surrounded by mounting holes), where the humid air enters from the bottom and leaves at the top. The dashed line marks the position of the CTA measurements. Additional point probe air velocity measurements have been performed at points on the long dashed and dotted line. The large black arrow shows the flow direction. Positions for the thermocouple pair are marked with a open square, pt100 positions for difference measurements are marked with a solid square [see also (Reichl et al. 2010)].

3.2 Measurement and Analysis Techniques

Several measurement techniques have already been applied (Reichl et al. 2010) to assess the temperature, flow and humidity conditions of the setup. Surface temperature and humidity sensors, heat sphere probes, CTA, PIV, thermography and image capturing techniques have been used. The test section surface temperature was scanned along horizontal and vertical lines using a fast reacting surface temperature probe with elastic thermo couple bands. For humidity and temperature measurements of the air flow downstream from the fans a standard room climate sensor was used. The velocity measurements have been performed using a heat sphere probe. The CTA scanning was based on a 3D traversing mechanism fully controlled by the acquisition computer. The CTA data was acquired using a 16 Bit 250 kS/s. Flow homogeneity tests have been performed using a 3D PIV consisting of one high speed camera and one camera using framegrabber technology. Both cameras were equipped with a 60 mm lens. An infrared heat image system was used for capturing the surface temperature of the aluminium test section plate. Image capturing was performed with a DV video camera equipped with a 120x objective using fixed white balance correction and manual focus. Promising results could be reached using a setup of six lamps using a blue LED with a luminosity of 50 cd producing a radiation angle of 12° by only introducing a total of 4.8 W power. Image acquisition was realized via the fire wire port direct link.

For an automated analysis of the video data the amount of available information from the videos has to be reduced. This was performed in the following steps: Firstly, one frame per second proved sufficient to cover the relevant processes. Secondly, the RGB values of each pixel are translated into the according hue-saturation-lightness (HSL) values and only the L value is kept. This has also been done for the images/frames of differences, where the difference between each considered frame and an initial reference frame is computed. Thirdly, the average lightness (0 = black, 1 = white) of all pixels contained in one region/tile is calculated and plotted against time (see Figure 3 as an example). From the lightness curves of the difference frames one can also automatically retrieve the starting time of condensation. Initially the difference-lightness attains of course a value close to 0, and when the condensation starts it rises very sharply. If one fits a continuous function (which is constant for t below tc and linear above) to the data until shortly after the sharp rise, one obtains the estimated condensation time tc with an error bar resulting from the noise-range. To obtain a similar procedure for the icing process there is still more effort necessary, since the lightness curves can behave very differently for the various considered surfaces.

3.3 Results

Application of the introduced experimental techniques yield the following results: The vertical temperature gradient is 0.2 °C, the horizontal temperature gradients depend on the position and ranges from 0.6 °C in the 'feed' line to 0.2 °C in the 'return' line (see Figure 1). The surface temperature follows the heat exchanger fluid temperature nicely with an offset of around +2.8 °C at -20 °C. Combining the information of the heat sphere probes, the CTA measurements and the 3D PIV analysis, the establishing flow patterns in the wind tunnel are given to be slightly asymmetric with higher values on one side of the wind tunnel. This effect, however, is only effective at higher fan power settings. For a typical fan power of 40%, the flow is homogeneous with a mean velocity of 2.3 m/s.

3.3.1 Stainless steel heat exchanger backplate

A thermocouple pair was positioned in the upper third of the measurement zone (open squares in Figure 1). Two resistor temperature dependent (RTD) pt100 have been placed up- and downstream of the measurement zone (see solid squares in Figure 1).

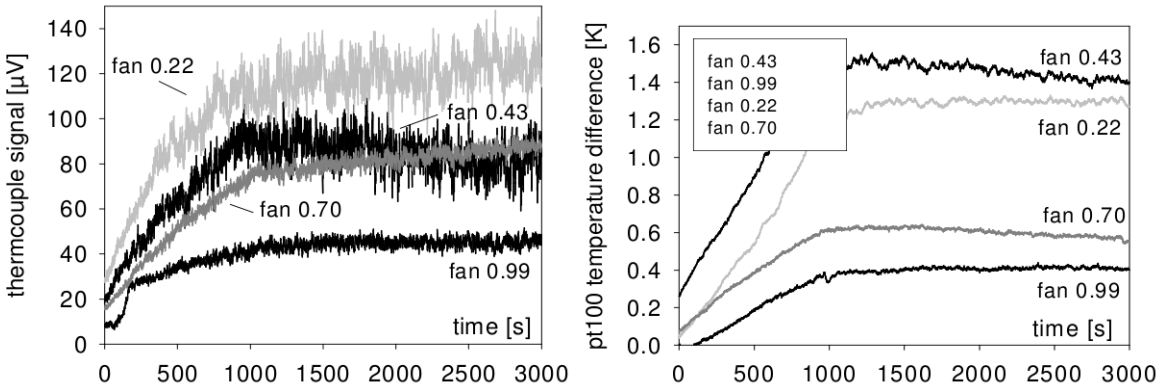

Figure 2. Thermocouple signal (left) and pt100 temperature difference (right) as a function of time for different flow speeds (ranging between 1 m/s and 8 m/s). The flow temperature was kept fix at 24 °C, the rel. humidity was 37%.

If the flow speed is reduced significantly (see Figure 2, left), the thermocouple signal increases. Higher flow velocities lead to smaller values of the thermocouple signal. The incoming air cannot be cooled to a large extent. A similar picture can be gained by using two pt100 RTDs. The upper two curves, however, change position in comparison to the thermocouple pair.

Measurements changing the relative humidity while keeping flow speed (2 m/s) and temperature (22 °C) constant have already been discussed in (Reichl et al. 2010). Computational image processing now allows for a more quantitative analysis (see Figure 3).

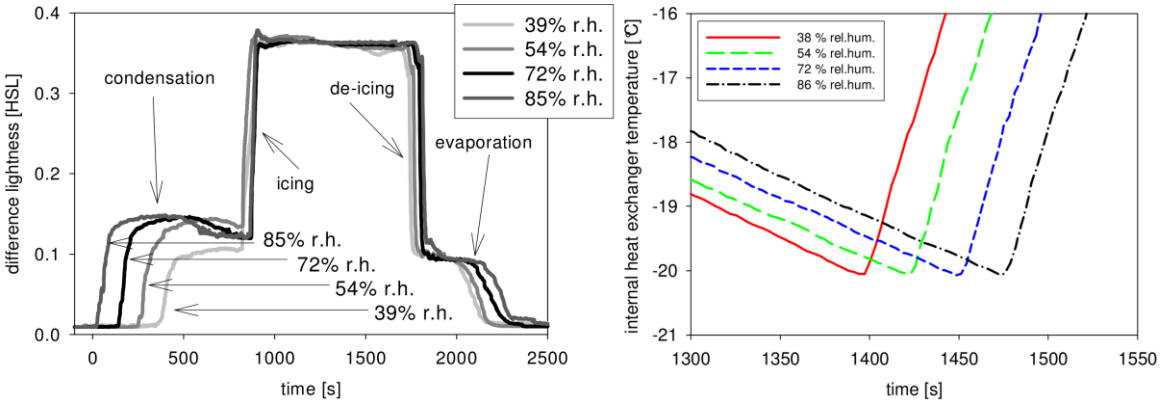

Figure 3. Difference lightness [HSL] signal of the condensation, icing, de-icing and evaporation processes (left) with varying rel. humidity, flow temperature ~22 °C, flow speed 2 m/s. The cooling curves of the heat exchanger fluid are showing the setpoint change times [right, (Reichl et al. 2010)].

Depending on the humidity (flow speed and temperature is fixed) condensation occurs separated in time. Icing and de-icing, however, can be extracted as a sharper process only separated by times in the range of 1-2 minutes. Evaporation occurs in reverse order to the condensation process.

3.3.2 Structured plates

In addition to a flat plate, three different micro structures have been selected (see Table 1).

Table 1. Definition of structured plates

plate 1	flat plate, no structure	plate 2	halfpipes with diameter 0.5 mm
plate 3	halfpipes with diameter 1 mm	plate 4	triangle with round bottom

Figure 4 shows the difference lightness revealing condensation and subsequent icing processes of the 4 different plates. The heat exchanger temperature was driven down to -30 °C. De-icing and de-fogging was reached by subsequently increasing the temperature to +50 °C (see dashed lines in Figure 4).

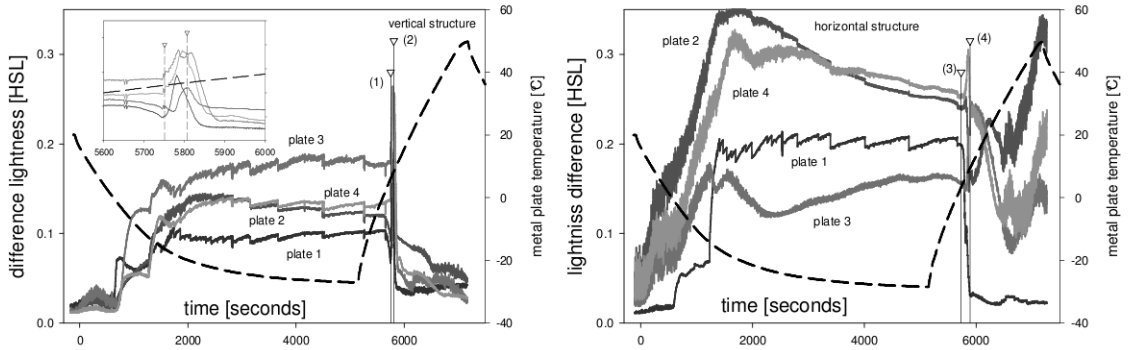

Figure 4. Difference lightness [HSL] signal of the phase change process on structured plates (left = vertical, right = horizontal structures). The dashed line shows the heat exchanger temperature (right scale). Rel. humidity ~60%, flow temperature ~12 °C, flow speed 2 m/s. Triangles with droplines correspond to the snapshots in Figure 5. A detailed view of full ice and de-fogging of the left figure is given in its insert.

The horizontally structured plates show larger noise, which can be attributed to the stronger reflectivity of these plates for the chosen light position. Vibrations of the plates due to the fans lead to increased levels of scattered light in this case. Significant shifts in icing times can be seen for the vertically structured plates separating for example plate 3 and plate 4 by approximately 300 seconds. It can be seen, that reflectivitiy changes in steps as ice is formed and ice growth takes place. The signal increase for the horizontal plates at 6500 seconds can be attributed to remaining water droplets and water structures on the plate (see also Figure 5). This effect can not be seen for the vertical plates, as water can run down the microstructure.

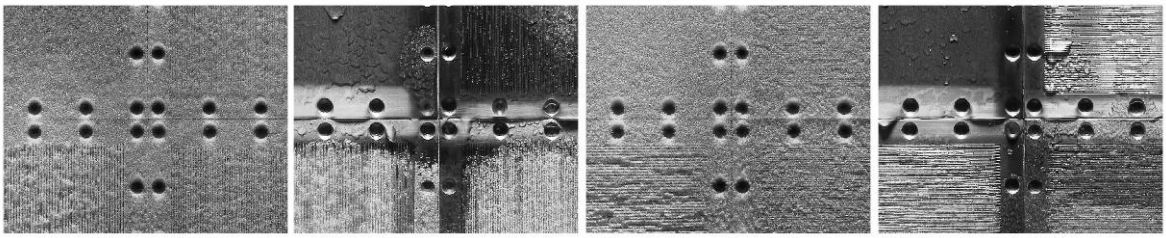

Figure 5. Icing and de-icing of vertical and horizontal structured plates. All four structures have been placed simultaneously on the backplate. First row = plate 1 (left) and plate 2 (right), second row plate 3 (left) and plate 4 (right).

3.3.3 Glasses with different surface structures

Table 2 introduces eight structured glass plates, whose contact angles range from 10° to 118°. The untreated glass plate (reference) has a contact angle of 20°.

Table 2. Glass structure specifications and contact angle with water of different glasses

Name {Number}	reference {1}	HMDS {2}	MC6 {3}	self-cleaning (TiO2) {4}	M5C6F3 {5}	MSL {6}	SiH {7}	nano-structured
contact	20°	70°	87°	10°	100°	102°	106°	118°

angle θ								

The wind tunnel setup was tilted, so that the glass surfaces faced downwards and enclosed an angle of approx. 40° with the horizontal.
Cooling the heat exchanger plate down to -5 °C, condensation and subsequent icing can be seen on the different glass structures (see Figure 6). By stopping the cooling process at 0 °C for a time span of approximately 1700 seconds and then increasing the temperature to +40 °C, condensation and evaporation can be studied (see Figure 6, left).

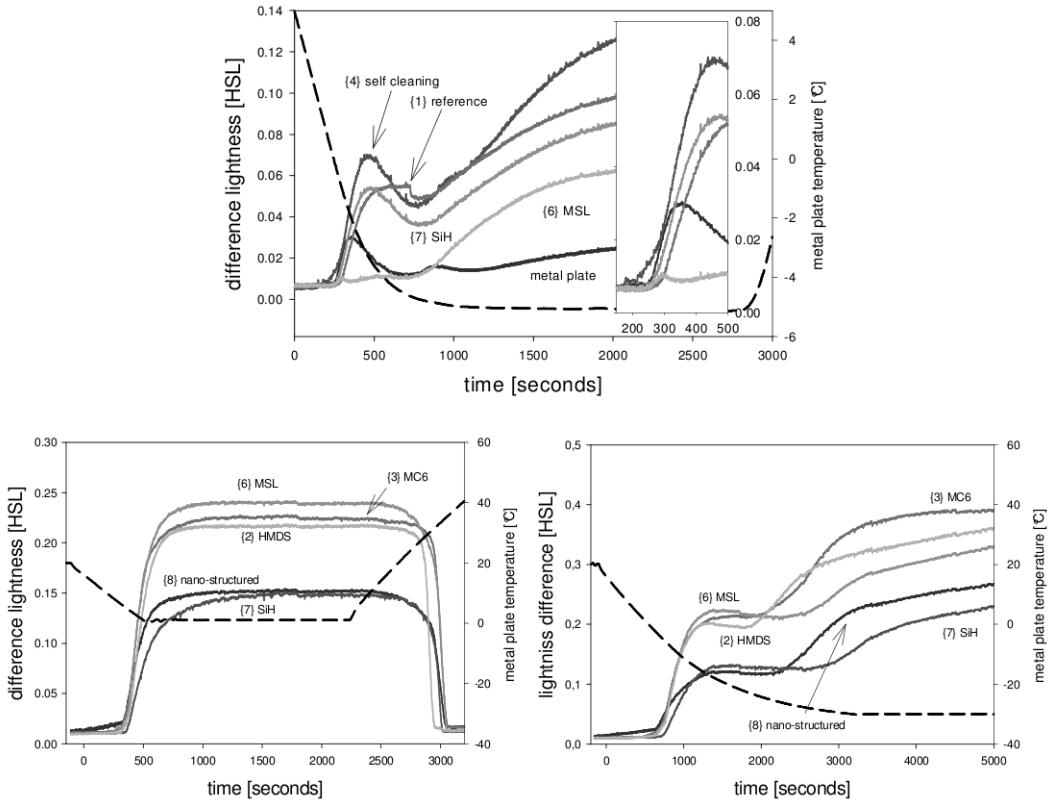

Figure 6. Difference lightness [HSL] signal of the condensation process on differently treated glass plates. The dashed line shows the heat exchanger temperature (right scale). Rel. humidity ~71%, flow temperature ~5 °C, flow speed 1 m/s (top); rel. hum. ~78%, flow temp. ~12 °C, flow speed 1 m/s (left); rel. hum. ~68%, flow temp. ~6 °C, flow speed 1 m/s (right).

The differences in the condensation and de-fogging times can be extracted from Figure 6. However, small errors due to variations in the backplate temperature and not evenly distributed heat conductive paste have to be considered. Icing processes (see Figure 6, right) seem to occur at significantly shifted times.

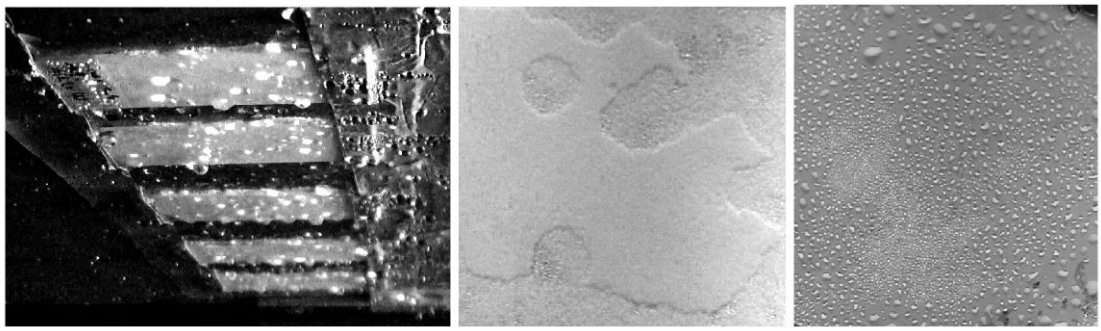

Figure 7. During de-icing on an inverse tilted setup (see Figure 4, right) drops are forming on the glass surfaces (left) – Water film and water droplets on glass surfaces (mid & right).

4 SIMULATIONS

Before going into the details of the specific method for simulating the onset of condensation and icing the underlying physical process, nucleation, has to be described and understood.

4.1 Nucleation Theory

Nucleation is a molecular phenomenon which can (directly) only be captured by molecular dynamics simulation [c.f. (Toxvaerd 2002)]. To be able to perform investigations on a larger scale a suitable and widely used method is classical nucleation theory (CNT) (Vehkamäki 2006). One of its features is, that the nucleating matter is considered continuous, usually in the form of an ideal gas. Also, via the definition of the so called surface of tension (where thermodynamic and mechanical surface tension coincide), an agglomeration of water molecules is simply describable as a spherical droplet of radius r. Even in equilibrium such a droplet is not unchanged, water molecules continuously accrete and evaporate to form a quasi-static condition. Also during nucleation processes, where the vapor pressure P_{v} is larger than the saturation vapor pressure $P_{\mathrm{v,sat}}$, both these events occur, and even then it may happen that very small droplets vanish again completely. However there exists a critical size of such droplets, which depends on the surrounding conditions (see below). Above this size the droplets will no longer vanish but only grow further, as long as the conditions are unchanged. A droplet of this critical size is called critical embryo; quantities referring to it are subsequently labeled with a star superscript.

The formation of such an embryo out of vapor costs (Gibbs free) energy $\Delta G^{\star}$ which is, according to CNT, proportional to the surface tension[1] and to the critical embryo volume $V^{\star}$ reciprocally proportional to its radius $r^{\star}$,

$$\Delta G^{\star} = \frac{\sigma V^{\star}}{r^{\star}} \,. \tag{1}$$

This formation energy represents a barrier to the nucleation process which reduces the rate J at which critical embryos occur per second per cubic meter:

$$J = J_0 \mathrm{e}^{-\frac{\Delta G^{\star}}{k_{\mathrm{B}} T}} \,, \tag{2}$$

where J_0 is the so called kinetic constant of nucleation, which also depends on material properties and surrounding conditions, k_{B} is the Boltzmann constant, and T is the temperature of the embryo. The supersaturation is derived from the saturation ratio $S = P_{\mathrm{v}}/P_{\mathrm{v,sat}}$, which is also termed relative humidity. Clearly, the nucleation rate is extremely sensitive to supersaturation. CNT also provides the expression for the critical embryo radius:

$$r^{\star} = \frac{2\sigma \mu_{\mathrm{H_2O}}}{\rho_{\mathrm{H_2O}} RT \ln S} \,, \tag{3}$$

where μ_{H2O} is the molar mass of water, ρ_{H2O} is the density of (liquid) water, R is the gas constant, and S is again the saturation ratio, which of course has to be larger than 1.

1 $\sigma = (0.117 - 0.000152\ T/\mathrm{K})\ \mathrm{N/m}$ between water and surrounding air

For heterogeneous nucleation at a flat surface the curvature (i.e., the radius) of the critical embryo is unchanged, but the volume is lowered. Since an ideal droplet at a flat surface resembles a spherical cap, the reduced volume hence only depends on the contact angle θ. After basic geometrical considerations one obtains

$$V_{\mathrm{het}}^{\star} = r^{\star 3}\frac{(1-\cos\theta)^2(2+\cos\theta)}{3}, \tag{4}$$

which reduces to the homogeneous value for the completely hydrophobic surface with $\theta = \pi$. When inserting the heterogeneous critical embryo volume into Equation (1) the same θ-dependence again occurs in the formation energy. Also, the kinetic constant of heterogeneous nucleation depends on the contact angle [a typical value would be $J_0 = 10^{26}\ \mathrm{m^{-2}s^{-1}}$ (Piucco et al. 2008)]. Using the direct vapor deposition model (Vehkamäki 2006) the heterogeneous nucleation rate, after tedious calculations given by

$$J = \sqrt{\frac{2\sigma\mu_{\mathrm{H_2O}}}{\pi N_{\mathrm{A}}}}\frac{1}{\rho_{\mathrm{H_2O}}}\left(\frac{P_{\mathrm{v}}}{k_{\mathrm{B}}T}\right)^2 \exp\left(-\frac{\Delta G_{\mathrm{het}}^{\star}}{k_{\mathrm{B}}T}\right)\frac{d_1}{S}\frac{(1-\cos\theta)^2\sqrt{2+\cos\theta}}{4} \tag{5}$$

(N_{A} being the Avogadro constant and d_1 the diameter of a water molecule), follows a similar trend like the homogeneous one, as can be seen in Figure 8.

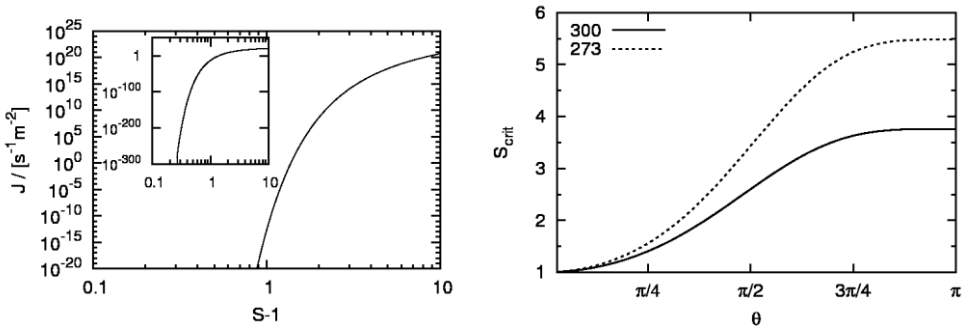

Figure 8. The dependence of the heterogeneous nucleation rate at T = 300 K and a contact angle of $\theta = \pi/2$ on supersaturation is visualized on the left side. The right panel displays the critical saturation ratio in dependence of contact angle for two different temperatures, as indicated in the legend.

If one makes the common choice for a critical nucleation rate (where a considerable amount of vapor condensates) of $J_{\mathrm{crit}} = 1\ \mathrm{cm^{-2}s^{-1}}$, one can calculate, for given temperature and contact angle, the respective necessary saturation ratio. Figure 8 (right panel) illustrates how this critical saturation ratio varies with contact angle. The value of $S_{\mathrm{crit}} = 1$ at $\theta = 0$ describes direct or film-like deposition of water molecules. Of course, these considerations can easily be repeated with the surface tension of ice.

4.2 Modified CFD Solver and Boundary Condition

As mentioned in the introduction it is intended to perform CFD simulations for the nucleation phenomenon of condensation. For this purpose a region similar to the test section of the experiments (see section 3.1) is set up, i.e., a rectangular duct of cross section $300\ \mathrm{mm} \times 100\ \mathrm{mm}$ and length $600\ \mathrm{mm}$. Air at $T_{\mathrm{air}} = 300\ \mathrm{K}$ and a velocity of $v = 2\ \mathrm{m/s}$ flows into the duct at one end and is exhausted against ambient pressure at the outlet. Initially it carries vapor at a mass concentration of $c_{\mathrm{m,v}} = 0.020\ \mathrm{kg/m^3}$, which is equivalent to a saturation ratio of $S = 0.8$.

As a first approach to humidity transport in air a simple scalar transport with diffusion is used for the mass concentration:

$$\frac{\partial c_{\mathrm{m,v}}}{\partial t} = -\mathrm{div}\,\mathbf{j} = \mathrm{div}\,\left(D_{\mathrm{v}}\,\mathrm{grad}\,c_{\mathrm{m,v}} - c_{\mathrm{m,v}}\mathbf{u}\right) \tag{6}$$

with a convective ($c_{\mathrm{m,v}}$ $\mathbf{u}$) and a diffusive (-D_{v} grad $c_{\mathrm{m,v}}$) part for the vapor flux $\mathbf{j}$. In OpenFOAM (http://www.openfoam.com/) this differential equation is simply introduced via the line

```
fvScalarMatrix cmvEqn(fvm::ddt(cmv)+fvm::div(phi,cmv)-fvm::laplacian(Dv,cmv));
```

and one additional variable (cmv) for the vapor mass concentration. The mass flow to the wall $\dot{m}/A$ (A is the area of the nucleating surface) due to critical embryo formation is simply given by the volume of the critical embryo $V^{\star}_{\mathrm{het}}$ times the density of the created water droplet times the nucleation rate J:

$$\frac{\dot{m}}{A} = V^{\star}_{\mathrm{het}}\rho_{\mathrm{l}_2\mathrm{O}}J \tag{7}$$

Since there is no convective mass flux through the surface, this vapor mass flow can directly be transformed into a condition for the gradient of vapor mass concentration

$$\mathrm{grad}\,c_{\mathrm{m,v}} = -\frac{\dot{m}/A}{D_{\mathrm{v}}}\mathbf{n}\,, \tag{8}$$

where $\mathbf{n}$ is the unit normal vector to the flow region at the surface of nucleation.

4.3 Results

If now one of the side surfaces of the rectangular duct is cooled, i.e., held at a constant temperature T_{surf} = 273 K < T_{air}, the conditions for measurable nucleation at this surface are met. For an initial laminar simulation of the flow one quickly obtains a stable condition for flow and temperature, where the temperature profile in a plane parallel to the flow direction and perpendicular to the cooled surface has the form given in Figure 9. One can clearly see the gradual cooling of the air as it flows over the cooled surface. If one also takes into account the loss of humidity due to the formation of critical embryos at the surface, there appears also a gradient in the water vapor concentration, although this change in humidity does not spread as fast as the one in temperature due to the considerably smaller (2 orders of magnitude) diffusion constant for humidity (see Figure 9).

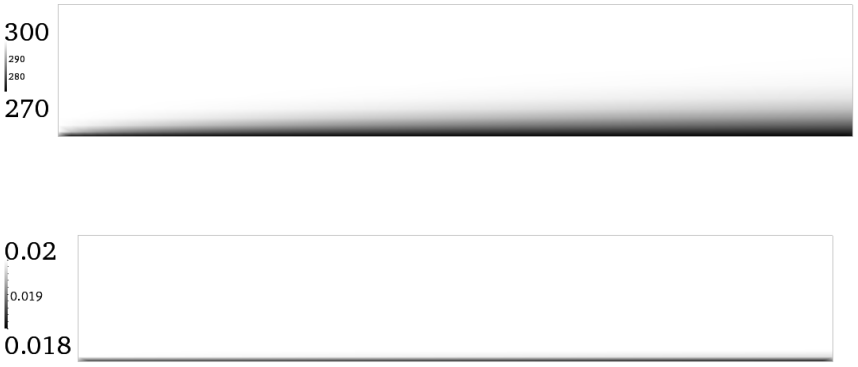

Figure 9. Temperature profile (upper panel, in K) and vapor concentration (lower panel, in kg/m^3) in a plane parallel to the flow and perpendicular to the cooled surface.

Since the Reynolds number of the described flow condition is of the order 10^4, a turbulent simulation is clearly necessary for a more realistic modeling of the situation. As a first step towards turbulence a standard *k-ε* model has been applied. While the profiles of temperature and vapor mass concentration are very similar in a plane like in Figure 9, there appears, in contrast to the laminar case, a spacial peculiarity. In the region very close to the cooled surface (i.e., the first calculation layer of the flow near the surface) the humidity loss becomes much more pronounced in the corners and at the end of the rectangular duct (see Figure 10).

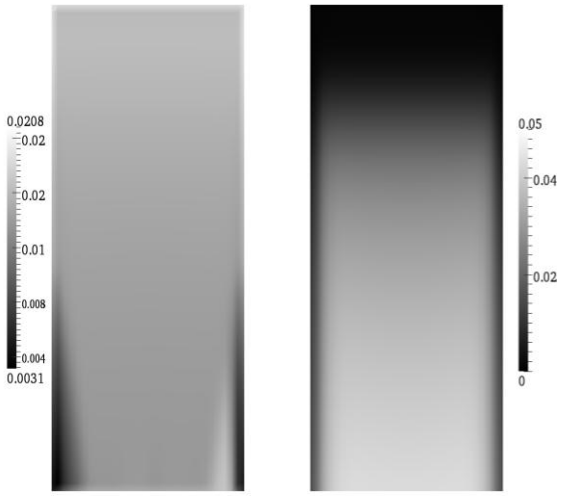

Figure 10. vapor mass concentration (left, in $\mathrm{kg/m^3}$) and turbulent kinetic energy (right, in J) close to the cooled surface.

Figure 10 gives a possible explanation for this effect: The turbulent kinetic energy k shows regions of low turbulence in the corners. The higher turbulence in the middle region may cause a better mixing of the humid air and hence a less pronounced humidity gradient.

5 CONCLUSION AND OUTLOOK

We presented a setup for studying phase-change processes on cooled plate surfaces, structured metal and glass surfaces. Measurements have been performed at different flow temperatures and different values of the relative humidity by placing the experimental test rig in a climatic chamber. A computational image analysis was presented and successfully applied to the available data. Metal plates with different microstructures show diverse patterns and times of icing and de-icing. Horizontally mounted, an increase in reflectivity due to remaining water droplets and water structures could be observed. Phase change processes on structured glass surfaces with different contact angles and UV transmissivity have shown, that condensation and evaporation occur in a smaller time range compared to the various ice formation stages, which are more separated. To further investigate the behavior of structured glasses, a significant increase in surface area seems to be necessary to avoid possible boundary effects. In addition to hydrophobic glass surfaces studies of more hydrophilic ones will be performed. The proposed methodology seems to be a promising option for accessing the occurrence of phase changes and the durations of the considered processes, to compare different surface structures of metals and glasses.

The obtained data were used as guidelines for the setup of first numerical simulation techniques, which showed promising results. The framework of classical nucleation theory has been extended to a model which can be incorporated into the open source CFD code OpenFOAM, which allows arbitrarily detailed further development. This will include the consideration of the influence of humidity on density and hence on the flow, using

generalized gas equations instead of the ideal gas one (for air and vapor), incorporating improved nucleation rates (respecting e.g. experimental corrections like for homogeneous rates or surface diffusion effects), modelling the influence of turbulence on the (vapor) diffusion coefficient, extending the simulations to transient conditions, considering the postnucleation droplet growth, creation of films, freezing of droplets/films and growth of ice. These investigations will finally lead to a detailed understanding of the phenomena concerning the nucleation of water vapor, and also the understanding of nucleation in general will benefit from the developed models and tools.

6 ACKNOWLEDGEMENTS

The authors like to thank Martina Jedinger for thorough proof-reading and corrections.

7 REFERENCES

Aljuwayhel N. F., D. T. Reindl, S. A. Klein, G. F. Nellis 2007. “Comparison of parallel- and counter-flow circuiting in an industrial evaporator under frosting conditions,” *International Journal of Refrigeration, Vol.* 30, Issue 8 pp. 1347—1357.

Egolf H. 1984. Grundlagen zur experimentellen Bestimmung der Bereifung von Luftkühlern, Dissertation ETH Zürich, Nr. 7509.

Lee K., S. Jhee, D. Yang 2003. “Prediction of the frost formation on a cold flat surface,” *International Journal of Heat and Mass Transfer,* Vol. 46, Issue 20, pp. 3789—3796.

Narhe R. D. and D. A. Beysens 2007. “Growth dynamics of water drops on a square-pattern rough hydrophobic surface,” *Langmuir,* Vol. 23, p. 6486.

Piucco R. O., C. J. Hermes, C. Melo, and J. R. B. Jr. 2008. “A study of frost nucleation on flat surfaces,” *Experimental Thermal and Fluid Science,* Vol. 32, p. 1710.

Reichl Ch., G. J. Pauschenwein, B. Windholz, B. Hebenstreit, and M. Monsberger 2010. "Experimental Studies on the Icing-Onset on Plates in Low Speed Flows," IIR 1st Conference on Sustainable Refrigeration and Heat Pump Technology, Stockholm.

Pauschenwein G. J., Ch. Reichl, B. Windholz, I. Moretti, and M. Monsberger 2010. "CFD Simulations For Solar Collectors Including Condensation And Ice Accretion," International Conference on Solar Heating, Cooling and Buildings, EuroSun.

Roy S., H. Kumar, R. Anderson 2005. “Efficient defrosting of an inclined flat surface,” *International Journal of Heat and Mass Transfer,* Vol. 48 Issue 13, pp. 2613—2624.

Shaw R. A. and D. Lamb 1999. ”Experimental determination of the thermal accommodation and condensation coefficients of water," *Journal of Chemical Physics,* Vol. 111, p. 10659.

Tassou S. A., C. J. Marquand 1987. “Effects of evaporator frosting and defrosting on the performance of air-to-water heat pumps,” *Applied Energy,* Vol. 28, Issue 1, pp. 19—33.

Toxvaerd S. 2002. “Molecular dynamics simulation of heterogeneous nucleation at a structureless solid surface," *Journal of Chemical Physics,* Vol. 117, p. 10303.

Vehkamäki H. 2006. Classical Nucleation Theory in Multicomponent Systems, Springer, Berlin Heidelberg. ISBN-10 3-540-29213-6, ISBN-13 978-3-540-29213-5.

Wu X., W. Dai, W. Xu, and L. Tang 2007. “Mesoscale investigation of frost formation on a cold surface”, *Experimental Thermal and Fluid Science,* Vol. 31, p. 1043.